PAPER

Check for updates

Interface engineering approach of in-air-processed Sb₂S₃ solar cells enabling 7.5% AM 1.5G device efficiency and an 18% indoor milestone performance

Hadeer Hussien, [ID] *[a] Malle Krunks, [ID] *[a] Nicolae Spalatu, [ID] *[a] Atanas Katerski, [ID] [a] Zacharie Jehl Li-Kao, [ID] [b] Sergio Giraldo, [ID] [b] Daniel Abou-Ras, [ID] [c] Arivazhagan Valluvar Oli, [ID] [d] Susanne Siebentritt, [ID] [d] Jonathan D. Major, [ID] [e] Aeshah A. Almushawwah, [ID] [ef] Thomas P. Shalvey, [ID] [e] Raitis Grzibovskis, [ID] [g] Aivars Vembris [ID] [g] and Ilona Oja Acik [ID] *[a]

Among the wide range of emerging absorber materials under development, Sb₂S₃, with its optimal bandgap of 1.7 eV and distinctive anisotropic properties, stands out as a material offering an excellent trade-off between intrinsic stability, cost-effective deposition, and high performance under both, AM 1.5G and indoor illumination. While current strategies focus on absorber optimization, interface engineering remains largely unexplored. In this work, we introduce, for the first time, a ZnO interfacial layer deposited *via* ultrasonic spray pyrolysis (USP) in air at the TiO₂/Sb₂S₃ interface. This innovation extends to a fully cadmium-free device architecture, in which all key layers—TiO₂ electron transport layer, ZnO interlayer, and Sb₂S₃ absorber—are processed entirely *via* USP under ambient conditions. A record efficiency of 7.5% under AM 1.5G illumination and an 18% indoor milestone performance is demonstrated for a TiO₂-based Sb₂S₃ solar cell platform, featuring a 150 nm thick absorber—the thinnest Sb₂S₃ absorber delivering such performance to date. Comprehensive characterization reveals the critical role of the ZnO interfacial layer, highlighting its impact on absorber grain size, interface and bulk defects, and device functionality. We propose refinements to indoor measurement protocols, accounting for variations in source temperature and incident power, paving the way for reliable indoor PV performance evaluation.

Introduction

The growing demand for advanced photovoltaic (PV) applications in modern society requires the development of energy materials and devices with customized properties. At this scale,

[a]Department of Materials and Environmental Technology, Tallinn University of Technology, Ehitajate tee 5, Tallinn, 19086, Estonia. E-mail: hadeer.saleh@taltech. ee; malle.krunks@taltech.ee; nicolae.spalatu@taltech.ee; ilona.oja@taltech.ee

[b]Electronic Engineering Department, Universitat Politècnica de Catalunya (UPC), Photovoltaic Lab – Micro and Nano Technologies Group (MNT), EEBE, Av, Eduard Maristany 10-14, Barcelona 08019, Catalonia, Spain

[c]Helmholtz-Zentrum Berlin für Materialien und Energie GmbH, Department Structure and Dynamics of Energy Materials, Hahn-Meitner Platz 1, 14109 Berlin, Germany

[d]Laboratory for Photovoltaics, Department of Physics and Materials Science Research Unit, University of Luxembourg, 41, Rue du Brill, L-4422 Belvaux, Luxembourg

[e]Stephenson Institute for Renewable Energy, Department of Physics, University of Liverpool, Liverpool, L69 7ZF, UK

[f]Department of Physics, Faculty of Science and Humanities in Al-Dawadmi, Shaqra University, Shaqra 11911, Saudi Arabia

[g]Institute of Solid State Physics, University of Latvia, Kengaraga Str. 8, Riga, LV-1063, Latvia

the emerging PV technologies must go beyond mere competitiveness with current established technologies in performance and reliability under the AM 1.5 solar spectrum. They should also drive expanded PV deployment by leveraging research expertise to address and embrace alternative applications, such as indoor photovoltaics (IPV). Thin-film technologies such as cadmium telluride (CdTe) and copper indium gallium selenide (CIGS) have been expertly designed to maximize power conversion efficiency (PCE) under the AM 1.5 outdoor solar spectrum, with an ideal bandgap around 1.4 eV. Yet, in the context of indoor applications, these cutting-edge technologies reveal significant limitations, as their performance is compromised by the fundamentally different illumination spectrum, highlighting an urgent need for innovative solutions tailored specifically for indoor energy harvesting. In recent years, there has been a focused and vigorous exploration of emerging photovoltaic materials, including organic, dye-sensitized, and perovskite solar cells (PSCs), which promise superior spectral matching for indoor applications. While performance exceeding 44% has been achieved under low-light conditions,[1,2]

This journal is © The Royal Society of Chemistry 2025

J. Mater. Chem. A, 2025, **13**, 37215–37231 | **37215**

and these materials benefit from low-temperature deposition processes and tunable properties, legitimate concerns remain regarding their overall long-term stability and, in the case of lead-based perovskites, their toxicity.[3] In this context, antimony sulfide (Sb_2S_3) has emerged as a promising inorganic PV absorber material for single-junction solar cells and as the top subcell in tandem solar cells. This is due to its exceptional intrinsic properties, including a high absorption coefficient ($\alpha > 10^4$ cm^{-1} in the visible region), a bandgap of 1.7 eV, excellent stability, and its abundant availability in nature.[4,5]

Given these advantages, Sb_2S_3 has the potential to enable resilient and low-cost IPV technology. Despite extensive research on Sb_2S_3 as a conventional PV absorber (leading to an impressive device PCE exceeding 8%, under AM 1.5 illumination),[6,7] demonstrating and validating the material's response to low-light and indoor illumination conditions remains a major focus within the research community. Fig. 1 illustrates the state-of-the-art efficiencies of Sb_2S_3 solar cells and recent efforts to demonstrate their operation under low-light conditions.[8–15] The corresponding devices information and their PV parameters under different illumination conditions are summarized in Table S1 in the SI. From Fig. 1, a few major aspects can be emphasised: (i) the majority of research efforts are dedicated to the development and optimization of Sb_2S_3 devices with a CdS electron transport layer (ETL), showing a breakthrough in both, AM 1.5 power conversion efficiency (AM 1.5-PCE) of ~8% (labelled with an orange star in the first box plot on the left[6,7]) and "indoor" power conversion efficiency (I-PCE) of ~20% (ref. 11) (forth box plot). (ii) For Cd-free Sb_2S_3/TiO_2 cell platforms, research efforts are significantly limited with a maximum

achieved AM 1.5-PCE of 7.08% (ref. 16) (blue filled star in the very right box plot) and a very recent demonstration of device operability under low light conditions with a maximum I-PCE of 11.26% under 1000 lux (3000 K LED source).[15] (iii) For both, CdS and TiO_2 device platforms, the improvements in PCE and I-PCE performance originate from the optimization of Sb_2S_3 absorber quality (including optimized grain growth control during deposition and/or applications of efficient post deposition treatments).[17–21] Thus, the engineering of the main interface (*i.e.*, incorporation of a suitable interface layer between Sb_2S_3 and the ETL) remains largely unexplored. Furthermore, the high discrepancy in Fig. 1 in presenting the I-PCE performances is likely to be related to the wide variety of indoor lighting scenarios, thus limiting the feasibility of direct comparison of indoor results between groups. This illustrates that there is a clear challenge in establishing a unified protocol for testing and validating I-PCE performance, and that a more holistic approach mapping various illumination scenarios is needed.

The cumulative results presented in Fig. 1 show that there is massive potential for Sb_2S_3 devices to make a disruptive breakthrough in the IPV field. Theoretically, the maximum PCE that could be achieved by a single-junction Sb_2S_3 solar cell is 28.64% with an open-circuit voltage (V_{OC}) of 1.402 V, a short-circuit current density (J_{SC}) of 22.46 mA cm^{-2}, and a fill factor (FF) of 91%, under 1-sun AM 1.5G illumination.[22,23] Under indoor conditions, however, a maximum theoretical PCE approaching 50% is possible owing to the improved matching between the bandgap and the indoor light source.[24,25] The deficiency in V_{OC} remains one of the major challenges, requiring identification of innovative strategies for absorber

Fig. 1 State-of-the-art efficiencies of Sb_2S_3 solar cells and recent efforts demonstrating their operation under low-light conditions. This highlights that the major efforts in the development of Sb_2S_3 solar cells are focused on the CdS based platform with demonstration of a record power conversion efficiency under standard test conditions (AM 1.5-PCE) of ~8% (ref. 6 and 7) (orange filled star in the very left box plot) and a record "indoor" power conversion efficiency (I-PCE) of ~20% (under 1000 lux, LED 3000 K).[11] The box plots on the very right, show the state-of-the-art PCE and I-PCE performances of the TiO_2/Sb_2S_3 device platform with the blue filled star marking the highest reported efficiency (7.08%)[16] and the red filled stars representing the performance indicators in this study, establishing a new record for TiO_2-based Sb_2S_3 solar cells under 1 sun illumination and competitive I-PCE values achieved with a very thin absorber thickness. Hollow blue and red stars refer to the previously reported AM 1.5-PCE and I-PCE at different illumination conditions, respectively.

37216 | *J. Mater. Chem. A*, 2025, **13**, 37215–37231

This journal is © The Royal Society of Chemistry 2025

and interface optimization in the device. To overcome these limitations, controlling the growth process of Sb_2S_3 crystals is crucial to improve film quality and device performance.[18,21,26] Drawing inspiration from previous experience, for instance with PSC, interface engineering has proven to be a critical approach for enhancing device performance, including under indoor illumination conditions.[27,28] For Sb_2S_3, previous studies have shown that the incorporation of ZnS,[29,30] $Zn(O,S)$,[31] and graphene nanoribbons[32] has high potential to suppress the interface recombination at the buffer/absorber interface while also enabling control over crystal orientation and film morphology. Considering these approaches, in this work we address the challenge of interface engineering in Sb_2S_3 solar cells,[33,34] by incorporating, for the first time, a ZnO interface layer by ultrasonic spray pyrolysis (USP) at the main interface between TiO_2 and Sb_2S_3. Our innovation lies in the development of a Cd-free device platform in which all key component layers in the cell stack (including, the TiO_2 ETL, ZnO interface layer, and Sb_2S_3 absorber) are processed using USP in an air environment. Considering our comprehensive results, we find that introducing an ultra-thin ZnO layer at the TiO_2/Sb_2S_3 interface primarily plays a morphological role. Specifically, the ZnO layer serves as a templating interface that critically influences the grain growth and size, with very little impact on the grain orientation of the Sb_2S_3 absorber. This represents a fundamentally different approach from conventionally reported dual-buffer layer configurations such as CdS/In_2O_3, SnO_2/CdS, or SnO_2/TiO_2 and CdS/TiO_2 in Sb-chalcogenide solar cells.[35–37] Furthermore, photoluminescence (PL) and surface photovoltage (SPV) measurements provide compelling evidence that the improvements observed in V_{OC} and overall power conversion efficiency (PCE) are attributable to the reduction in non-radiative recombination, occurring both at the TiO_2-ZnO/Sb_2S_3 interface and within the bulk absorber grown on the ZnO templating layer. This is in agreement with the XPS based band alignment, suggesting that ZnO has an impact on interface recombination suppression. These findings directly support the notion that while the ZnO layer was initially introduced for interface engineering, it yields benefits from both structural and electronic perspectives.

A competitive PCE of 7.5% was achieved under AM 1.5G (100 mW cm^{-2}), marking a new record performance for TiO_2-based Sb_2S_3 solar cells. It is worth mentioning that the absorber layer in our champion device has an average thickness of approximately 150 nm, which is about 35% thinner than that of devices with the highest globally recorded efficiencies.[6,7] Despite this reduced thickness, the device exhibited an impressive J_{SC} of 17.9 mA cm^{-2} (18.4 mA cm^{-2}, highest value), surpassing recently reported values in the literature for devices with thicker absorber layers.[6,7,16,20] The interface engineering, achieved through ZnO insertion, not only enhanced the J_{SC} but also significantly improved the V_{OC} from 686 mV to 729 mV. PL studies confirmed that the improvement in V_{OC} is attributable to a reduction in non-radiative recombination at the interface between TiO_2 and ZnO. Furthermore, we performed a comprehensive indoor measurement to explore the influence of ZnO on the indoor efficiency of Sb_2S_3 solar cells, using a novel and more

holistic approach considering a wide array of lighting scenarios in terms of both source temperature and incident power. By reporting surface plots of performance under a range of realistic illumination condition, we assess the resilience of the devices and find that cells incorporating interfacial ZnO are not only more efficient under all applied indoor illumination conditions, but also more resilient to low injection conditions. Under maximum injection conditions, an outstanding indoor efficiency of 18.2% was obtained under a 6000 K white LED illumination power density of 6200 μW cm^{-2}, highlighting the remarkable capability of Sb_2S_3 solar cells to maintain high efficiency even in indoor environments. Finally, various realistic use-case scenarios are considered by introducing a new type of diagram in which both the IPV and IoT devices can be simultaneously represented, illustrating the practical applications of our technology. These results underscore the promising potential of Sb_2S_3 solar cells for indoor PV applications, where optimizing performance under reduced light is crucial.

Results and discussion

Morphological and structural properties of ultrasonic-sprayed Sb_2S_3 films employing a ZnO interfacial layer deposited at different temperatures

The primary focus of this work was to identify whether an interface engineering approach, *via* inclusion of a ZnO interface layer on top of the TiO_2 ETL layer, could yield higher device performance. A key starting point was to determine if the addition of the ZnO layer modified the grain structure and ribbon orientation of the Sb_2S_3 films. As noted earlier this is crucial not only for overall film coverage but also due to the role of anisotropy in the carrier transport of the film. In this context, the first approach was to screen and understand the effect of ZnO deposition temperature on the morphology and structure of the Sb_2S_3 absorber. For this purpose, the USP deposition of ZnO was kept constant at 70 cycles, while the deposition temperature was varied from 350 to 500 °C.

The surface morphology of Sb_2S_3 films grown on TiO_2 and on TiO_2 coated with ZnO over 70 cycles at different temperatures was characterized by field emission scanning electron microscopy (FE-SEM) as shown in Fig. 2a–e. SEM images reveal slight improvement in film coverage, particularly for films prepared with ZnO deposition temperatures of 400 °C and 450 °C. The small white grains were identified as uncovered TiO_2 regions. These uncovered TiO_2 areas are attributed to the high roughness of the FTO surface. During film fabrication, TiO_2 conforms to the FTO surface texture, while Sb_2S_3 fills the cavities, forming a regular and smooth surface. However, since the absorber thickness does not exceed 100 nm under the previously described deposition conditions, parts of the TiO_2 surface remain uncovered (see SEM images in Fig. S1a and b in the SI). Additionally, energy-dispersive X-ray (EDX) spectroscopy analysis was performed on two distinct regions, spot 1 (white grain area) and spot 2 (completely covered area), as shown in Fig. 2f (see Fig. S1b and d in the SI). The results indicated a higher Ti content in spot 1 (white grain) compared to spot 2, while the Sb content was higher in spot 2 than in spot 1, confirming our
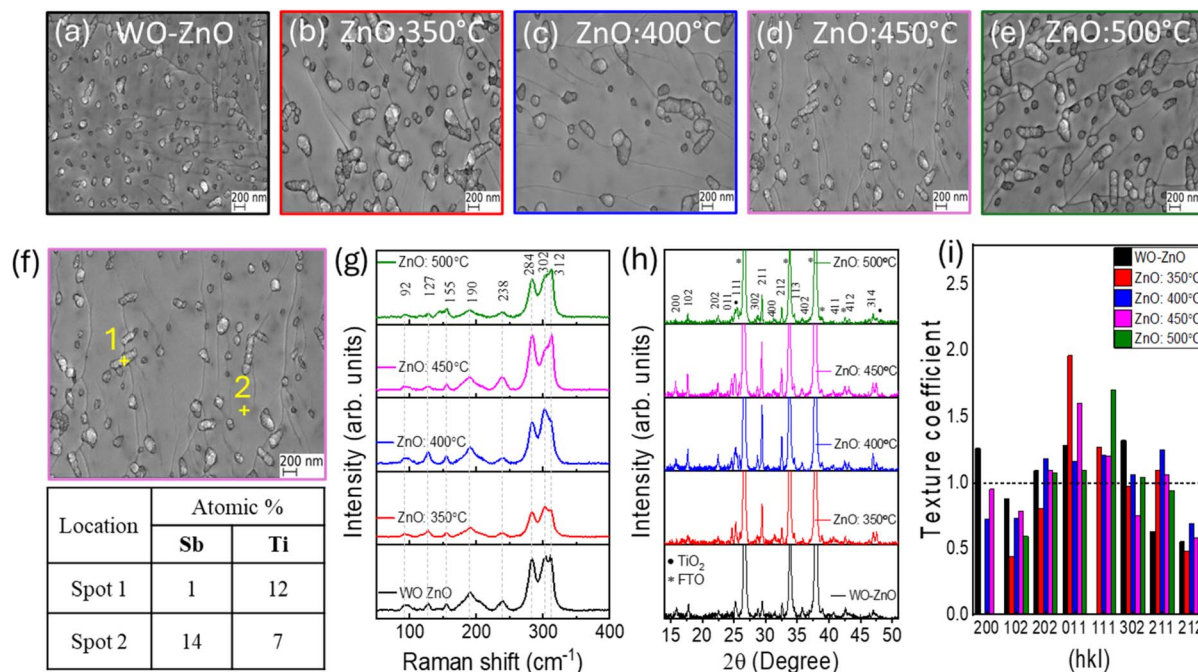
This journal is © The Royal Society of Chemistry 2025

J. Mater. Chem. A, 2025, **13**, 37215–37231 | **37217**

Fig. 2 (a–e) Top-view scanning electron microscopy (SEM) images of Sb_2S_3 thin films prepared directly on top of the TiO_2 ETL, and after the incorporation of the ZnO interface layer deposited with a fixed 70 spraying cycles at different temperatures ranging from 350 °C to 500 °C, respectively. (f) EDX analysis conducted for uncovered and covered areas on the TiO_2/ZnO: 450 °C/Sb_2S_3 stack surface. (g) Raman spectra, (h) XRD patterns and (i) texture coefficient of dominant diffraction patterns, of crystalline Sb_2S_3 films deposited on a 70-cycle ZnO interface layer sprayed at different temperatures.

observation that the white grains correspond to uncovered TiO_2 areas. Despite the presence of uncovered TiO_2 areas which act as pinholes in the absorber layer, the devices (both with and without ZnO deposited at different temperatures) show very good performance at this stage. In this context, we would like to provide a more detailed explanation of how these uncovered areas could affect device operation. In thin-film solar cells, several types of "pinhole" interfaces can form, including direct contact between the transparent conducting oxide (TCO) and the HTL or metal back contact; TCO or ETL with the absorber; and absorber with the metal contact. The electrical nature of these interfaces (whether ohmic or non-ohmic) depends on the conductivity and relative band alignment of the materials involved. In our case, exposed TiO_2 regions are in direct contact with the hole transport layer (P3HT), forming a non-ohmic interface.[38] While such pinholes may act as localized leakage paths, their impact on overall device performance is not governed solely by area fraction. Previous experimental studies have shown that the use of HTL is crucial for controlling non-ohmic shunting losses.[38,39] Additionally, the electrical properties of the surrounding absorber domains play a critical role in current distribution.[40]

These factors modulate the extent to which the pinholes affect key parameters like V_{OC} and FF, without necessarily inducing a full device shunt. In the next sections, we will address the impact of absorber coverage on device performance.

Furthermore, the phase composition of crystalline Sb_2S_3 films was studied by using Raman spectroscopy and XRD technique. Raman spectra obtained with a laser excitation

wavelength of 530 nm are depicted in Fig. 2g. The spectra display eight peaks at frequencies of 92, 127, 155, 190, 238, 284, 302, and 312 cm^{-1}. The absence of any Sb_2O_3 secondary phase confirms the successful formation of a single stibnite phase, further supported by XRD data. The detected peak at 238 cm^{-1} arises from S–Sb–S in-plane bending vibrations, while the out-of-plane S–Sb–S bending mode occurs at 190 cm^{-1}. The low frequency vibration modes observed at 155 and 92 cm^{-1} are associated with lattice modes. The peaks centred at 284, 302, and 312 cm^{-1} correspond to the stretching vibrational modes of Sb–S. Fig. 2h shows the evolution of XRD patterns of crystalline Sb_2S_3 films as the deposition temperature of ZnO increased from 350 °C to 500 °C. The detected diffraction peaks can be assigned to orthorhombic stibnite with *Pnma* 62 space group (JCPDS 01-075-4012). These peaks correspond to (200), (102), (202), (011), (111), (302), (211), (212), and (402) planes. To quantitively evaluate the degree of preferred crystallographic orientation, the texture coefficient (TC) is calculated using the Harriss equation.[41] As depicted in Fig. 2i, the TC values of the 011, 111, and 211 diffraction peaks all exceed 1.0 regardless of the ZnO deposition temperature, reaching a maximum of 2. This suggests that the ZnO deposition temperature has only a slight impact on crystallite orientation, with no evidence of preferential orientation, as later confirmed by pole figure measurements (see Fig. 5 b and d). Additionally, the Scherrer equation was used to estimate the size of coherently scattering domains in Sb_2S_3 from the 211 diffraction peak,[42] which increased from 34 nm to 46 nm as the ZnO deposition temperature was raised from 350 °C to 450 °C (see Table S2 in the SI).

37218 | *J. Mater. Chem. A*, 2025, **13**, 37215–37231

This journal is © The Royal Society of Chemistry 2025

Surface composition of TiO₂/ZnO and TiO₂/ZnO/Sb₂S₃

The next step involves optimizing the fabrication of the ZnO layer by varying the number of spraying cycles from 20 to 270 cycles, in increments of 50 cycles, while maintaining a fixed deposition temperature of 450 °C. This process aimed to evaluate how variation in ZnO spraying cycles affect the device performance. The deposition temperature of 450 °C was selected based on the solar cell output parameters obtained in the previous step (see the SI, Fig. S2, S3 and Table S2). This temperature is also preferred to avoid the transformation of TiO_2 from the anatase phase into rutile,[43] as the anatase phase is generally favored in photovoltaic applications due to its good electron mobility and stability.[44] At the same time, this temperature ensures sufficient energy for the proper formation of ZnO.[45] At this point, it is worth mentioning that ZnO was deposited *via* ultrasonic spray pyrolysis using a 1 : 2 molar ratio of $ZnCl_2$ to thiourea precursor solution (5×10^{-4} M, $ZnCl_2$). While this precursor combination is usually used to deposit ZnS,[46] our deposition conditions namely the air environment, low concentration of thiourea, high deposition temperature, and the catalytic effect of the underneath TiO_2 layer, prevented the formation of ZnS. Instead ZnO was formed, as confirmed by XPS analysis. As shown in Fig. 3a Ti 2p exhibited two peaks, Ti $2p_{3/2}$, and Ti $2p_{1/2}$, located at 459.4 eV and 465.1 eV respectively. The intensity of these peaks decreased while the intensity of Zn $2p_{3/2}$ and Zn $2p_{1/2}$ characteristic lines, at 1022 eV and 1045 eV, respectively, gradually increased with the increasing number of ZnO spraying cycles as shown in Fig. 3b. The binding energy difference between two lines is 23.0 eV, indicating the existence

of Zn^{2+}.[47,48] Fig. 3c shows the characteristic peak of O 1s, which consist of two components centred at 529.8 eV and 531.5 eV. These peaks are ascribed to M–O and surface hydroxyl groups, respectively.[48,49] These findings are consistent with previous reports of ZnO deposited on TiO_2 surfaces.[50–52] Additionally, XPS spectra of Sb 3d, and S 2s for the Sb_2S_3 film deposited on TiO_2 coated with ZnO over 150 cycles are given in Fig. 3d and e. The binding energy at 539.1 eV is ascribed to the Sb $3d_{3/2}$ core level of Sb_2S_3,[53] while the peak centered at 225.8 eV corresponds to the S 2s level in Sb_2S_3.[54]

Impact of ZnO thickness variation on Sb₂S₃ solar cell characteristics

In this section and based on the previous findings, sets of devices were fabricated with varying ZnO thickness as a function of spraying cycles ranging from 20 to 270 cycles. A schematic representation of the planar superstrate device architecture of FTO/TiO₂-ZnO/Sb₂S₃/P3HT/Au along with the current density–voltage (J–V) curves of champion devices with and without the ZnO interface layer, under standard AM 1.5G illumination is illustrated in Fig. 4a and b. The PV parameters of Sb_2S_3 solar cells employing different ZnO interlayer spraying cycles and pristine TiO_2 are summarized in Table 1. The variation of ZnO spraying cycles was intended to achieve superior improvement in solar cell performance. The PCE significantly improved from 5.6% to 7.5% after the insertion of a 150-cycle ZnO interface layer. To our knowledge, this represents the highest efficiency reported for TiO₂/Sb₂S₃ solar cells. This enhancement is primarily due to the increase in V_{OC} from
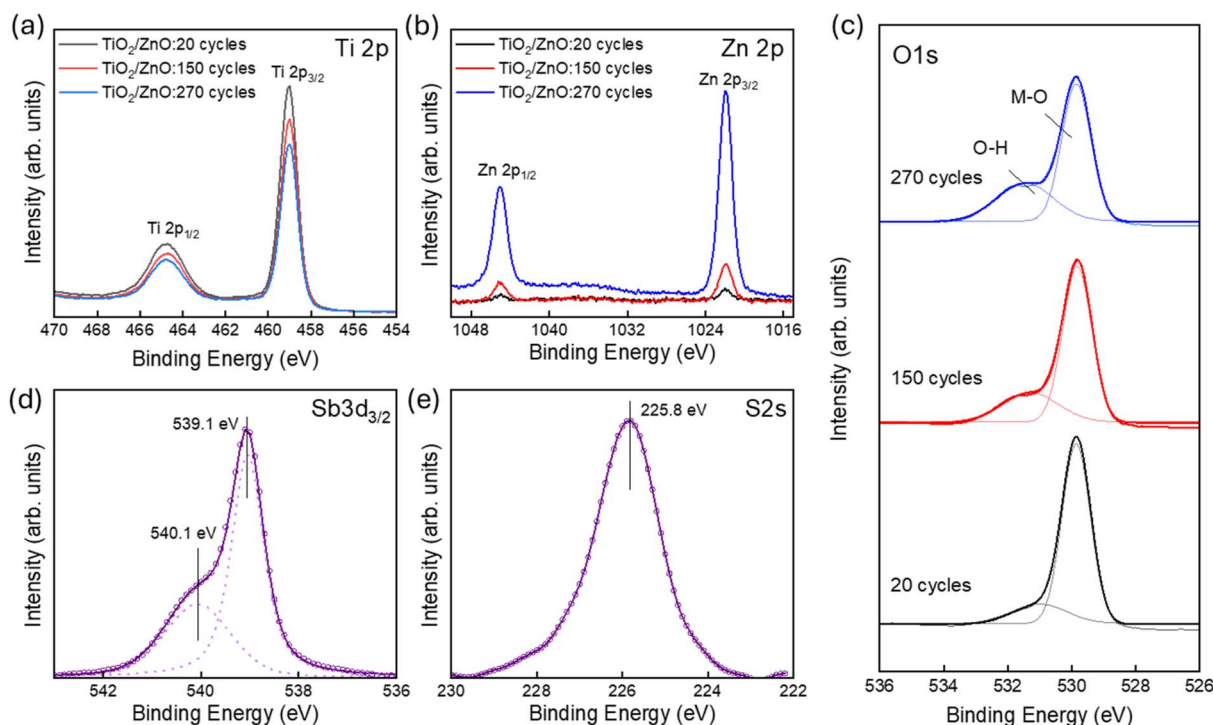

Fig. 3 (a) Ti 2p, (b) Zn 2p and (c) O 1s XPS spectra corresponding to an un-cleaned surface of TiO₂ coated with ZnO over 20, 150 and 270 cycles. (d and e) High-resolution XPS spectra corresponding to Sb 3d and S 2s of Sb₂S₃ films deposited on top of ZnO over 150 cycles.
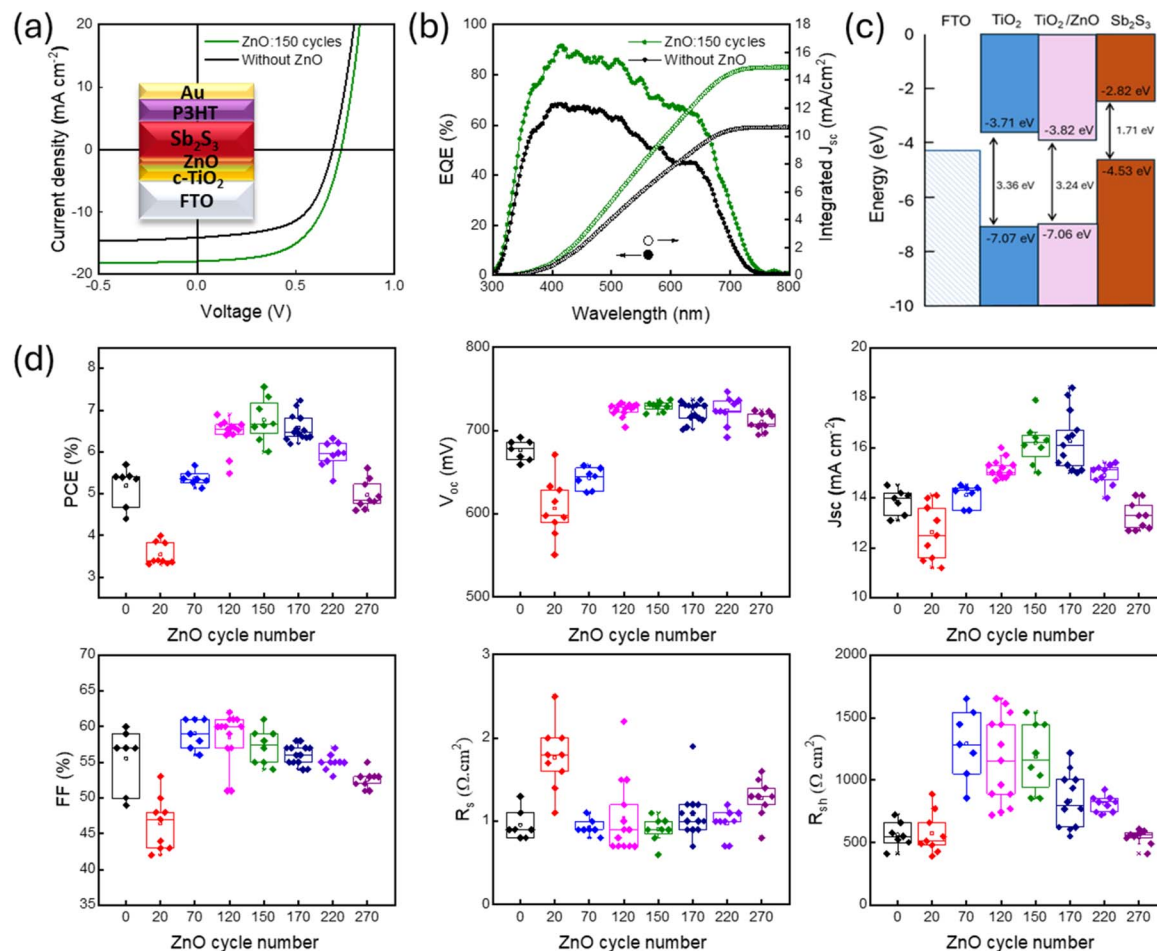
This journal is © The Royal Society of Chemistry 2025

J. Mater. Chem. A, 2025, **13**, 37215–37231 | **37219**

Fig. 4 (a) Current density voltage (J–V) curves and (b) EQE spectra and integrated photocurrent of champion devices for both the pristine TiO$_2$ ETL and with ZnO deposited at 450 °C under illumination power of 100 mW cm^{-2}, respectively. The inset in figure (a) shows a schematic diagram of the device architecture: FTO/TiO$_2$/ZnO/Sb$_2$S$_3$/P3HT/Au. (c) Band alignment diagram of TiO$_2$/ZnO/Sb$_2$S$_3$ interfaces, band positions determined from XPS analysis of the device surfaces. (d) Statistical box plots of the obtained PV parameters based on various ZnO spraying cycles (for at least seven devices).

Table 1 Photovoltaic performance parameters of the champion Sb$_2$S$_3$ solar cells with and without the ZnO interface layer, measured under 100 mW cm^{-2} illumination power

Device	V_{OC} (mV)	J_{SC} (mA cm^{-2})	FF (%)	PCE (%)
Without ZnO	686	14.1	59	5.6
ZnO-20 cycles	590	14.1	48	3.9
ZnO-70 cycles	658	14.2	61	5.6
ZnO-120 cycles	731	15.3	62	6.8
ZnO-150 cycles	729	17.9	58	7.5
ZnO-170 cycles	719	18.4	55	7.2
ZnO-220 cycles	737	15.1	57	6.3
ZnO-270 cycles	718	14.1	53	5.3

686 mV to 729 mV and J_{SC} from 14.1 mA cm^{-2} to 17.9 mA cm^{-2}. To verify the reliability of this improvement, a statistical analysis was conducted on the device parameters, including PCE, V_{OC}, J_{SC}, and FF for at least 7 devices, as represented in Fig. 4d. The photovoltaic parameters derived from ZnO-based devices are superior compared to those of control devices. The

increment in V_{OC} values is strong evidence for better interfacial contact between TiO$_2$ and Sb$_2$S$_3$ after the insertion of ZnO. Additionally, the dramatic rise in shunt resistance associated with the utilization of ZnO indicates a significant mitigation of shunt pathways.

To elucidate the origin of these performance improvements, we further analysed the charge transport and recombination processes through dark J–V characteristics and impedance spectroscopy (see Fig. S4 in the SI). The ZnO-based device shows a lower reverse saturation current density (4.3×10^{-7} vs. 1.6×10^{-6} mA cm^{-2}) and reduced ideality factor (~1.65). For both devices, the ideality factor $n > 1$, indicating that Shockley–Read–Hall recombination is dominant.[55] Impedance Nyquist plots further showed a higher recombination resistance for the device including ZnO (2246 vs. 1894 Ω), confirming that the ZnO interlayer effectively suppressed carrier recombination in the space charge region and/or at interfaces.

The observed drop in PCE after increasing ZnO spraying cycles up to 270 cycles can be attributed to the decrease in both shunt resistance and the fill factor compared to the values

37220 | J. Mater. Chem. A, 2025, 13, 37215–37231

This journal is © The Royal Society of Chemistry 2025

obtained when using 120–220 cycles. More likely at this stage, the thicker ZnO layer has a deleterious effect on the growth of Sb_2S_3, as the crystallite size decreases from 48 nm to 39 nm when the number of spraying cycles increases from 150 to 270 (see Table S4 in the SI). We further measured the external quantum efficiency (EQE) spectra for champion devices, both control and with the ZnO layer. As illustrated in Fig. 4b, the ZnO based device shows a higher spectral response with a maximum EQE value of 91% at 420 nm, and an integrated J_{SC} of 14.9 mA cm^{-2} against 10.6 mA cm^{-2} for the reference device, demonstrating that photogenerated carriers are effectively dissociated in the active layer followed by more efficient electron transfer to the FTO through the TiO_2/ZnO layer.[56]

As mentioned above, incorporation of a 150-cycle ZnO layer at the interface resulted in a significant increase in all PV parameters. To understand the role of the ZnO interface layer from the perspective of band alignment (efficiency of the charge transport at the main interface) we performed additional XPS analysis based on the secondary electron cutoff (SEC) and valence band maximum (VBM) and proposed the energy band diagram for the TiO_2/ZnO/Sb_2S_3 interface (Fig. 4c). Our analysis suggests a cliff-like interface alignment between the TiO_2 ETL and the Sb_2S_3 absorber, and the inclusion of ZnO seems to have a moderate impact on adjusting this effect. It is important to mention that the survey and core level analysis showed a large presence of Ti 2p on the sample surface, resulting in stronger TiO_2 signals when probing the SEC and VB compared to ZnO. This effect created challenges in clearly distinguishing the VB and WF values of TiO_2 and ZnO. This indicates that the ZnO interface layer is either extremely thin or non-conformal. Considering this for the ZnO layer we relied on electronic parameters reported in the literature.[57,58] Interestingly the reported VB and WF values in the literature suggest that in fact, inserting a continuous ZnO layer at the interface does not promote favourable band alignment. From this point of view, one could not expect improved charge transfer at the interface. However, our results suggest that inclusion of ZnO by USP suppresses interfacial recombination (which would be more challenging for the cliff alignment) while still remaining thin and discontinuous enough, to allow tunnelling of the charge carriers at the main interface.

To provide better understanding of how the microstructure of the Sb_2S_3 layer can affect this enhanced performance, electron backscatter diffraction (EBSD) maps were acquired. As shown in Fig. 5a–d, the insertion of the ZnO interlayer slightly modified the in-plane (X–Y) grain orientations. Moreover, the average grain size of the Sb_2S_3 layer increased from 0.9 μm to 1.4 μm. Larger grains and thus, a smaller density of grain boundaries increases the lifetime of the minority-charge carriers and consequently the V_{OC} of the solar cell. Moreover, the insertion of the ZnO interface layer notably influenced the thickness of the Sb_2S_3 layer as visible in the cross-sectional SEM images (Fig. 5e). This stack exhibits a thicker Sb_2S_3 absorber layer of 150 nm, compared with only about 100 nm in the reference film, despite both undergoing the deposition with a fixed 40 cycles of the absorber precursor. Such behavior aligns with the known anisotropic growth characteristics of Sb_2S_3 depending on the

underlying surface.[17] This could also explain why the J_{SC} is larger for the device stack with the intermediate ZnO layer. However, it is worth noting that, in this particular case (having ZnO underneath the Sb_2S_3 absorber layer), improved device performance was achieved with an absorber thickness larger than 100 nm (the reference absorber thickness in this study). This contrasts with our previous attempts, where increasing the absorber thickness from 100 nm to 150 nm without incorporating the underlying ZnO layer, despite achieving full absorber coverage, did not enhance performance but rather resulted in a deterioration of the PV parameters, especially J_{SC} and FF.[59] This highlights the dual functionality (structural and interface defect passivation) of the ZnO interface layer allowing the integration of a thicker Sb_2S_3 absorber layer with improved properties, resulting in enhanced device performance.

As discussed above the presence of pinholes in the absorber can be expected to contribute to shunting pathways in the device. In our case, the optimized USP-deposited TiO_2 platform enables high-quality, conformal coverage even on slightly rough FTO, and thus in our device structure, the ohmic contact between FTO and Sb_2S_3 is excluded. However, in cases where pinholes are present in the absorber, several studies have shown that the choice of the hole transport layer (HTL) becomes critical in controlling the non-ohmic shunting losses in Sb_2S_3 and Sb_2Se_3 solar cells, particularly as it relates to the presence of absorber pinholes, which in turn depends on the deposition route and tuning process.[38,39] Thanks to a well-standardized HTL protocol and a reliable baseline reference cell architecture, we show that even with some pinholes in the absorber, the impact of the ZnO interfacial layer on both the structural and electrical properties of Sb_2S_3 and related interface properties, as well as on the overall device performance, can be clearly decoupled and highlighted. SEM images (Fig. 5e) showed a clear improvement in the absorber coverage when comparing the surface morphology of the ZnO-based film to that of the reference film. This reduction in exposed TiO_2 regions is consistent with the observed improvements in both V_{OC} and FF. These findings are in line with previously reported simulations involving similar TiO_2/P3HT interfaces, which demonstrated that increasing the pinhole area fraction leads to a decrease in V_{OC} and FF.[38] Collectively, our results indicate that the benefits of introducing a ZnO interlayer extend beyond electronic band alignment to include a significant morphological impact, which plays a critical role in enhancing Sb_2S_3 absorber quality and overall device performance.

Although the growth mechanism of Sb_2S_3 on TiO_2/ZnO is not yet fully understood, we propose a tentative explanation that extends our previously reported Sb_2S_3 growth mechanism on TiO_2,[60] supported by the analysis of our current results and the cumulative effects observed. Crystalline Sb_2S_3 typically forms through a two stage process: in the first stage, amorphous islands develop via the Volmer–Weber (island) growth mode during ultrasonic spray pyrolysis at 185 °C, where the high surface energy drives the formation of discrete 3D islands that expand vertically and laterally on the TiO_2 before coalescing into a continuous layer.[60] Crystallization then occurs in the second stage during rapid annealing at 270 °C under nitrogen,

Published on 09 d'octubre 2025. Downloaded on 29/1/2026 8:30:25. This article is licensed under a Creative Commons Attribution-NonCommercial 3.0 Unported Licence.
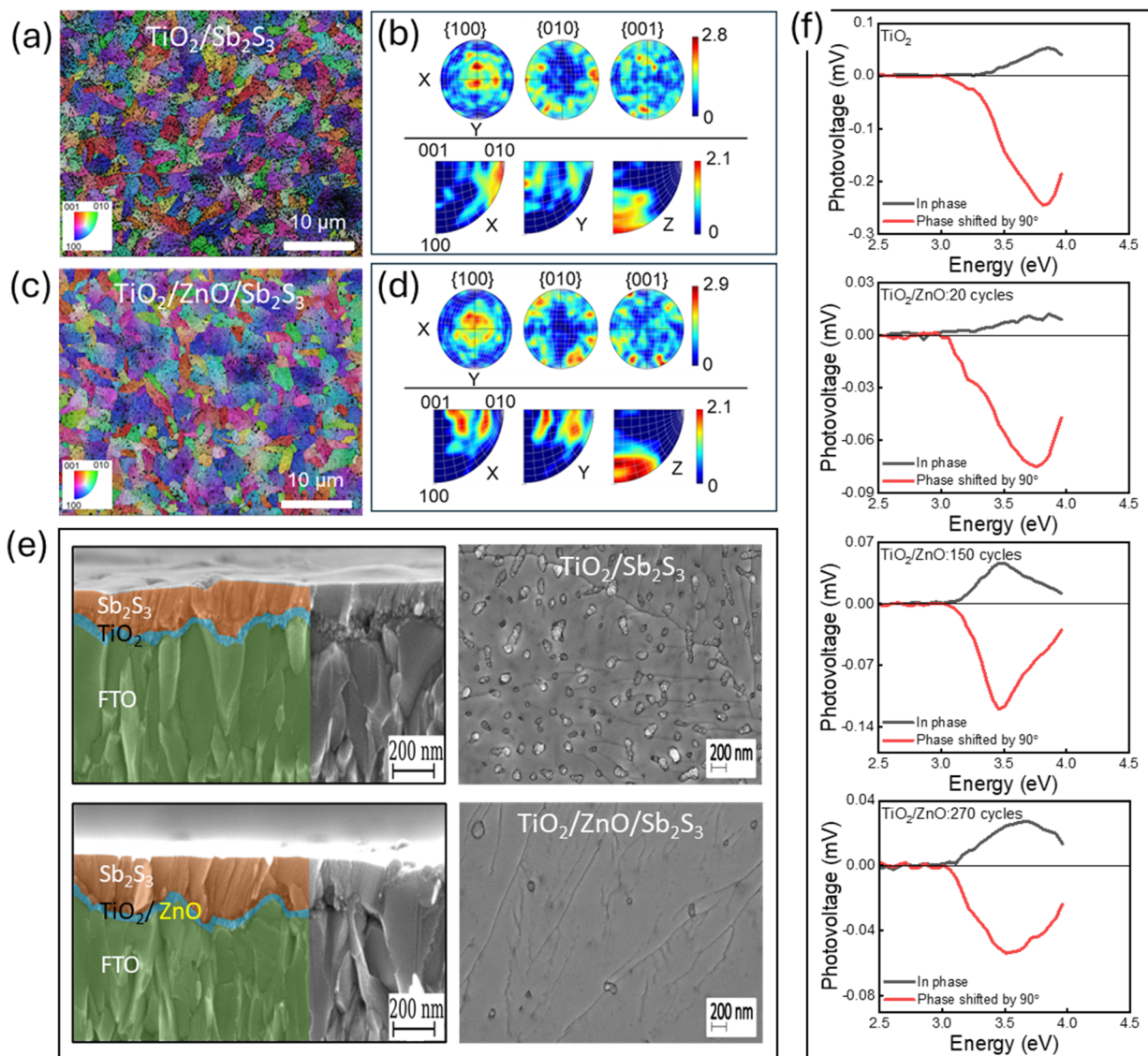
Fig. 5 EBSD orientation distribution maps (in which the local orientations are represented by false colors, see legend), as well as the corresponding pole figures and the inverse pole figures acquired on the crystalline Sb$_2$S$_3$ deposited on TiO$_2$ (a, b) and TiO$_2$ coated with ZnO deposited over 150 cycles (c, d), respectively. Cross-section and surface SEM images of Sb$_2$S$_3$ thin films prepared directly on top of TiO$_2$ surface and after the incorporation of a 150-cycle ZnO interface layer deposited at 450 °C. (e) SPV in phase and phase shifted by 90° signals of the bare TiO$_2$ surface and TiO$_2$ coated with ZnO layers deposited using 20, 150 and 270 cycles (f).

leading to the formation of a polycrystalline absorber layer. Along with these growth stages, the initial nucleation is strongly governed by the surface/interface chemistry of the underlayers. On one hand, XPS O 1s spectra (Fig. 3c) confirm the presence of surface OH groups in all ZnO coatings, which may contribute to increased surface polarity and hence to decreased surface/interface energy.[61] However, if one relies only on the implication of OH, then the effect of 270-cycle ZnO cannot be fully described.

This leads us to hypothesize that, under this condition, the 150 cycle ZnO provides an optimal balance between surface polarity, coverage, and morphology, effectively reducing the interfacial free energy and enhancing the work of adhesion.[61,62]

According to heterogeneous nucleation theory, this reduction lowers the barrier *via* a smaller contact angle θ, thereby

promoting the formation of fewer but larger and more stable islands in the first stage.[63,64] Subsequent annealing at 270 °C drives their crystallization, during which strong coalescence occurs because the rate of material transfer between larger islands is high. Orientation selection becomes more pronounced in this stage, driven by the minimization of interfacial and surface energies. As a result, large grains with lower surface energies grow predominantly in lateral directions, leading to the formation of a dense, continuous Sb$_2$S$_3$ absorber film, while still exhibiting a largely random grain orientation. A similar effect has been reported for a very thin Ce$_2$S$_3$ interlayer at the CdS/Sb$_2$S$_3$ interface, where the reduction of interface energy facilitated heterogeneous nucleation, leading to larger grains and more uniform films.[20]

37222 | *J. Mater. Chem. A*, 2025, **13**, 37215–37231

This journal is © The Royal Society of Chemistry 2025

Furthermore, we performed modulated SPV to gain deeper insights into the role of ZnO in enhancing V_{OC}. The SPV technique can provide valuable insights into the surface properties concerning both fast and slow processes in relation to the modulated period. The in-phase (x-signal) and 90° phase-shifted (y-signal) SPV signals correlate with the fast and slow responses, respectively. Positive (or negative) x-signals indicate the preferential separation of electrons towards the bulk (or surface). Furthermore, the sign of the y-signal, in comparison to the x-signal, gives more information about the preferential direction of trapped charges. If x and y signals have opposite signs, it indicates that both trapped and fast separated charges are directed in the same direction. Fig. 5f depicts the modulated SPV spectra of the in-phase and 90° phase-shifted signals, measured for pristine TiO_2 and TiO_2 coated with ZnO deposited over 20, 150 and 270 cycles. The in-phase signals are positive for all the samples, revealing that photogenerated electrons preferentially separate towards the internal interface, consistent with the fact that TiO_2 and ZnO are intrinsically n-type semiconductors.[65,66]

The SPV response of pristine TiO_2 shows a redshift in the onset energy of the y-signal compared to the x-signal; this can be attributed to the slow discharge of deeper defect states. However, this shift was not observed after depositing ZnO at 150 and 270 cycles, validating the effectiveness of ZnO in passivating the defect states in the TiO_2 layer and as a result, improving the quality of the TiO_2/Sb_2S_3 interface. The corresponding bandgap (E_g) of pristine TiO_2 and 150-cycle ZnO coated TiO_2 was determined to be 3.36 eV and 3.24 eV employing the squared SPV-amplitude signal (Fig. S6, SI).

To better understand the increase in V_{OC} we studied absolute PL spectra of a sample without a ZnO layer and a sample with 150-cycle ZnO. The non-radiative loss in these samples is still very high, such that under 1 sun equivalent excitation no PL from the samples was detected. Using higher laser power and a focussing lens, so that the excitation flux density reaches approximately 160 suns, the PL spectra in Fig. 6 were obtained. The maxima are at 1.58 and 1.57 eV, much lower than the band edge of 1.81 eV extracted from the inflection point of the EQE spectra in Fig. 4c. However, the EQE onset is rather gradual, partly due to the reduced thickness of the absorber films and partly due to bandgap fluctuations and tail states, in which case the PL maximum can be shifted much lower than the band gap.[67,68]

To check if the observed luminescence originates from the absorption edge or if it is rather due to tail states, we use the relation between the luminescence spectrum and the EQE, based on the reciprocity principle:[68,69] $\phi_{PL}(E) \sim EQE(E)\phi_{bb}(E)$, where ϕ_{bb} is the black body spectrum. These "reconstructed PL spectra" are also shown in Fig. 6. It can be seen that the maxima of the measured PL spectra are close to those of the reconstructed PL spectra. We therefore assume that the measured PL spectra are indeed due to states near the absorption edge and not due to defects. Then we can use the PL quantum efficiency Y_{PL} to estimate the non-radiative V_{OC} loss from $kT \ln Y_{PL}$ to be about 660 mV and 720 mV for the sample with and without ZnO, respectively. From the derivative of the EQE spectra with respect
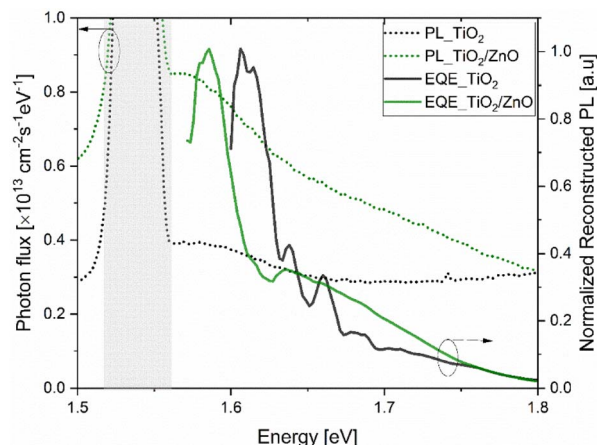

Fig. 6 PL spectra measured under approximately 160-sun excitation, together with the normalised PL spectra extracted from the EQE spectra. The grey box marks the second order of the exciting laser. The PL quantum efficiency is estimated to be 10^{-11} and 10^{-12}, for the sample with and without ZnO, respectively.

to E we can estimate the width of the effective band gap distribution σ.[70] This width is related to the radiative loss of V_{OC} via $\Delta VOC^{rad} = \sigma^2/(2qkT)$. The EQE spectra in Fig. 4c yield a width of the band gap distribution of 73 meV, resulting in a radiative loss of about 100 mV. Because of the very gradual increase of the EQE spectra at the absorption edge the radiative loss cannot be neglected. Taking the Shockley–Queisser V_{OC} of the bandgap (1.5 V) and subtracting the radiative and non-radiative losses, we reach a V_{OC} of 740 mV and 680 mV, for the samples with and without ZnO, respectively, very close to the best measured V_{OC} (Table 1). We can thus conclude that the improvement in V_{OC} is entirely due to a reduction in the non-radiative recombination at the TiO_2 and ZnO interface and/or in the bulk of the absorber, grown on the different interfaces.

Deep level transient spectroscopy analysis

Deep level transient spectroscopy (DLTS) analysis was used to interrogate the electrically active defect content in the highest efficiency device produced with a ZnO interfacial layer. DLTS analysis was primarily developed for analysis of single crystal materials with Schottky contacts. In these structures well-defined single defect peaks are typically observed and the "standard" maxima analysis approach for the determination of defect properties for a selection of rate windows, is easy and highly accurate.[71] For thin film heterojunction devices there is a significantly higher degree of complexity, and while this approach is still possible it can be prone to systematic errors.

The standard DLTS maxima analysis approach is only valid for single non-overlapping levels which produce an exponential decay transient. Due to the limited energy resolution of the maxima analysis approach, it can be unsuitable where multiple overlapping levels cause non-exponential decay transients. Instead, the defect content can be identified by directly evaluating the decay transient to identify the time constants and amplitudes of the multiple emission processes occurring at
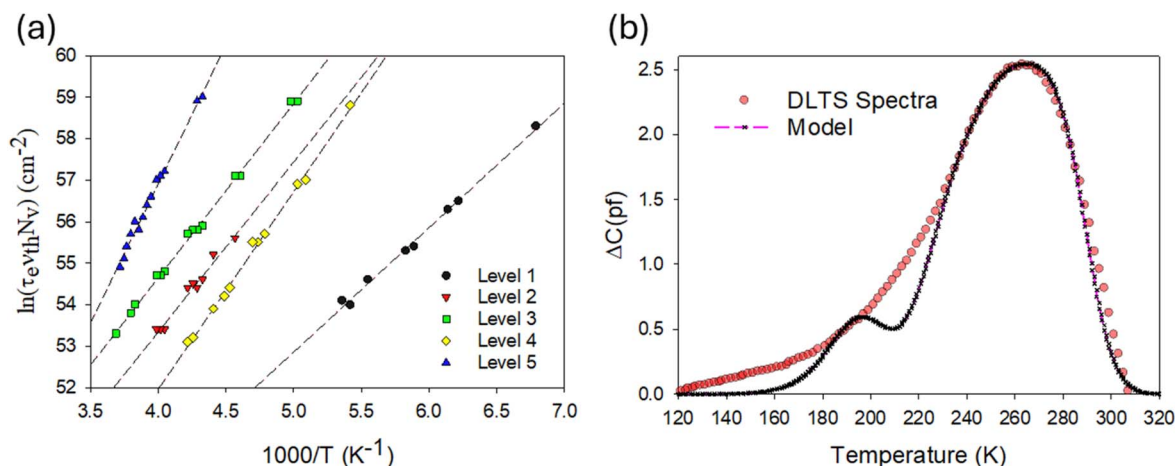
This journal is © The Royal Society of Chemistry 2025

J. Mater. Chem. A, 2025, **13**, 37215–37231 | **37223**

Fig. 7 DLTS analysis of the champion device (a) Arrhenius plots for deep levels extracted *via* multi-exponential fitting to decay transients across three-period width measurements (20 ms, 200 ms and 500 ms), (b) complete modelled DLTS spectra using all levels with their respective weightings, superimposed on the DLTS spectra of the champion device.

each temperature. This can be done either *via* a Laplace style analysis[72] or by discrete level estimation based on a multi-exponent fit. While both approaches were applied here, the multi-exponent fit using S. Provencher's DISCRETE algorithm[73] was found to produce more reliable data. The Arrhenius plots for identified defects are given in Fig. 7a with associated trap energy values and capture cross sections given in Table 2. Because it is possible to fit multiple combinations of exponentials to a particular decay transient, the validity of extracted data needs to be established with reference to a physical model.

A set of 5 defect states were identified in the 265–581 meV range, all of which are likely to act as centres for non-radiative recombination and ultimately limit performance. The modelled responses of each individual defect were then calculated and a composite fit was produced by weighting the concentration of each defect (Table 2). The validity of the determined levels was then established *via* comparison of the outputted DLTS spectra (capacitance change, ΔC, for a given "rate window" *versus* temperature) with the modelled data, given in Fig. 7b. We note at this point that we quote normalised weightings rather than absolute trap density values, N_T, which are often quoted in DLTS analysis. Trap density is determined by scaling the magnitude of the capacitance changes against shallow doping density, determined from capacitance–voltage measurement. There can be significant variations in both these terms due to unrelated capacitive effects for thin film heterojunction devices such as these (*e.g.* contacting and interface

charge accumulation).[74] Hence, we elect to forgo the unreliable absolute values in favour of a normalised ratio approach.

The recorded DLTS spectra show a clear main peak position, one which is very broad and with a non-symmetric tail, indicative of multiple defect peaks contributing to the spectra. The composite fit suggests that the main peak observed is composed of levels 2–5, with an additional contribution to the low temperature tail from level 1. While the fit around the main peak is of good quality, there are clear gaps in the fit at 200–220 K and <180 K. This suggest that there are additional defects producing signals in these ranges, but despite multiple attempts it was not possible to identify these levels. A limitation of DLTS is that it cannot directly interrogate the source of electrically active defects. Instead reference to density functional theory (DFT) calculations of defect formation energies offers the most reasonable route for defect identification.

For Sb_2S_3 this is highly challenging. Because of the material's low crystal symmetry, each defect type results in multiple associated trap states spread throughout the bandgap.[75] Indeed, given the variety of defects that occur within the 265–581 meV range, and the associated uncertainty when compared to calculations simulated at 0 K, we cannot definitively state whether the defects result from antisite or vacancy defects of either type. However, irrespective of the nature of the defects observed, and performance benefits delivered *via* the additional interface layer, their impact as recombination centres suggests that improved material quality for Sb_2S_3 is achievable. If these defects can be engineered out of the device, further performance gains beyond the current state of the art would be eminently possible.

Indoor performance validation: refinements to indoor measurements

For indoor photovoltaic performance evaluation, a direct comparison is proposed between the control device and below 1000 μW cm^{-2}. While peak efficiency reaches 11.2% under indoor conditions (incident power in the 1500–3000 μW cm^{-2}

Table 2 Trap energy (E_T) and capture cross section (σ_P) values from Arrhenius fitting along with weightings used to fit the DLTS spectra

Defect level	E_T (meV)	σ_P (cm^{-2})	Weighting
1	265	5.6×10^{-17}	0.09
2	352	8.8×10^{-17}	0.11
3	360	3.6×10^{-17}	0.33
4	408	4.5×10^{-15}	0.19
5	581	1.0×10^{-13}	0.28

37224 | *J. Mater. Chem. A*, 2025, **13**, 37215–37231

This journal is © The Royal Society of Chemistry 2025

range), it quickly drops well below the 10% threshold and approaches the 5% value when incident power is below 500 μW cm^{-2}. For an incident power of 46 μW cm^{-2} (T = 4000 K), the efficiency drops down to a value of 4.02%. At this point, it is useful to introduce a resilience factor, that is the ratio between the highest and lowest efficiency, taken at a fixed temperature (in this case, we choose T = 4000 K), and between the incident power densities of ∼3000 μW cm^{-2} and ∼50 μW cm^{-2} respectively. This resilience factor R^{4000} is in this case equal to R^{4000} = 4.02/10.55 = 0.38. This indicate a poor resilience to changes in the lighting scenarios and would be a problem for powering IoT systems under normal operating conditions.

The device including interfacial ZnO (Fig. 9), on the other hand, shows much higher resilience to low incident power densities. Starting from a higher peak value of about 15.5% for power densities in the 1500 μW cm^{-2} incident power density range, the device remains above 13% for an incident power density down to 200 μW cm^{-2} and remains at 12.3% for an incident power of 50 μW cm^{-2} (T = 4000 K). This illustrates an impressive resilience and usability range for this sample. Referring again to the previously introduced resilience factor between 3000 μW cm^{-2} and 50 μW cm^{-2}, it corresponds to R^{4000} = 0.78, that is, an IPV system with a very consistent performance record for the device with a 150-cycle ZnO interfacial

layer. Rather than focusing on specific lighting conditions, which would improperly represent the reality of indoor illumination, we propose instead a more holistic approach where both source temperature and incident power are varied within a range typical of common environments, and the PV figures of merit are presented in the form of surface plots. The illumination conditions are summarised in Table S5a and b in the SI.

The PV parameters as a function of illumination conditions are reported in Fig. 8 for the control device, and the device including interfacial ZnO in Fig. 9. The general trend is very similar in both cases, that is, with voltage, current and fill factor nearly independent of the source temperature. This is expected considering the bandgap of Sb$_2$S$_3$ situated very near the optimal value, with an excellent spectral matching for lighting scenarios from 3000 K to 6000 K. In terms of peak values however, and dependence on incident power density, a clear difference is observed between the device including interfacial ZnO and the control device. Indeed, we observe that in the absence of ZnO (Fig. 8), the FF and V_{OC} are far less resilient to low incident power densities, resulting in a fast degradation of performances irrespective of the lighting conditions. For this record sample, when increasing the power density to 6200 μW cm^{-2}, a case corresponding to the maximum power density measured in the office space of the Polytechnique University of Catalonia,
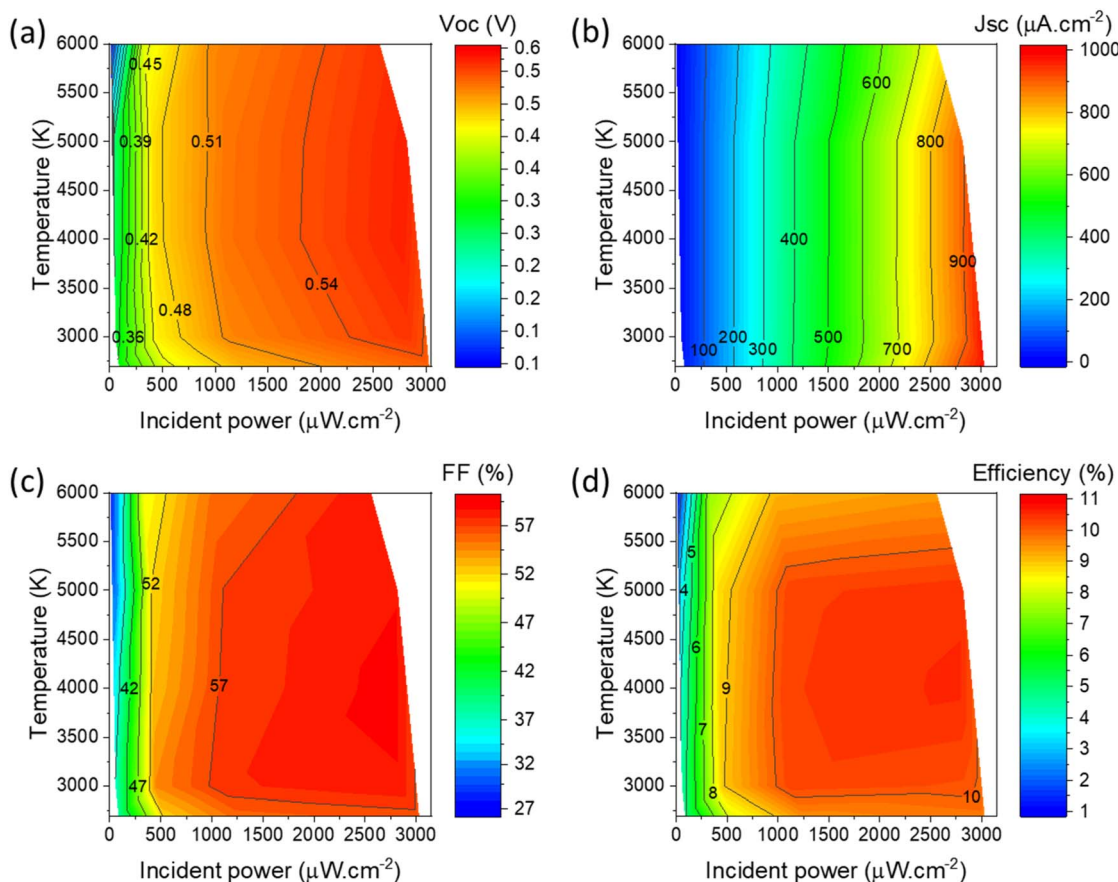

Fig. 8 Surface plot of the PV figures of merit for the sample without interfacial ZnO where the incident light power density (x-axis) and source color temperature (y-axis) are simultaneously varied: (a) open circuit voltage, (b) short circuit current density, (c) fill factor, and (d) power conversion efficiency.
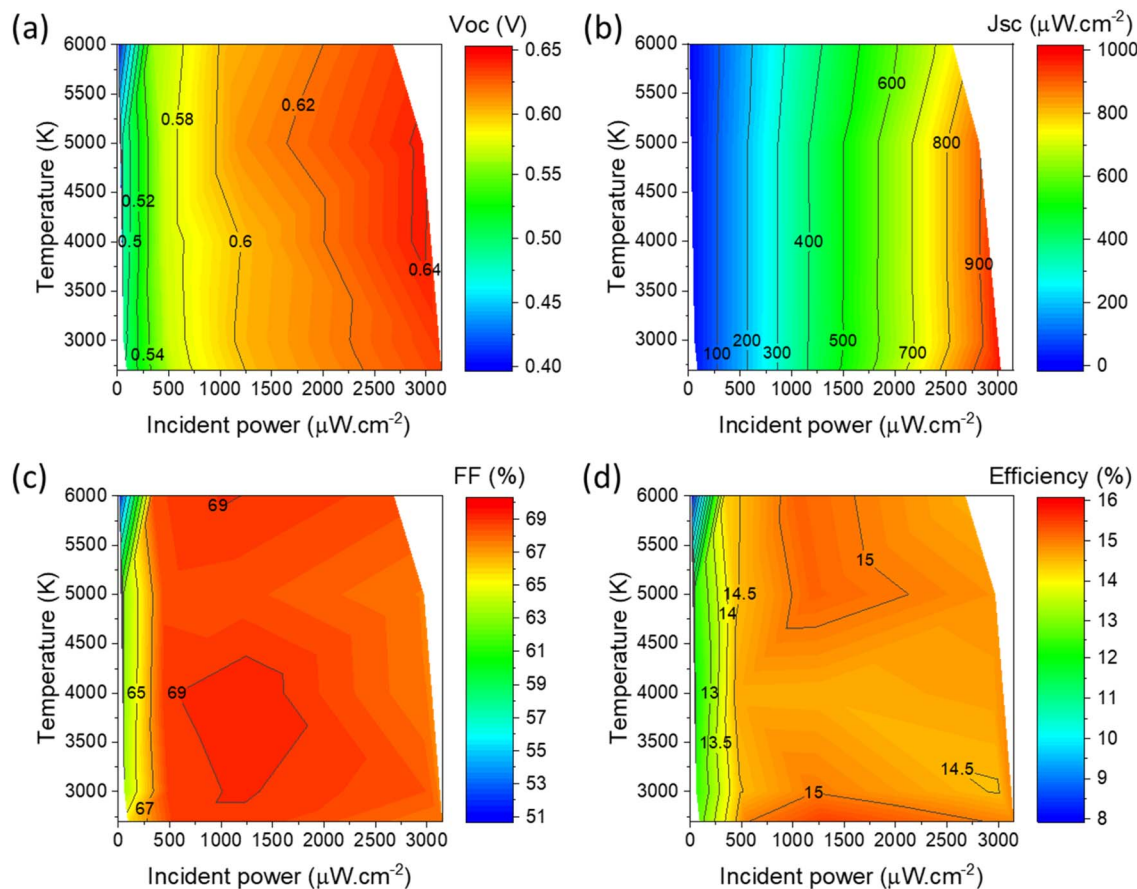
This journal is © The Royal Society of Chemistry 2025

J. Mater. Chem. A, 2025, **13**, 37215–37231 | **37225**

Fig. 9 Surface plot of the PV figures of merit for the Sb_2S_3 solar cell including a 150-cycle ZnO interfacial layer where the incident light power density (*x*-axis) and source color temperature (*y*-axis) are simultaneously varied: (a) open circuit voltage, (b) short circuit current density, (c) fill factor, and (d) power conversion efficiency.

a maximum efficiency of 18.2% is reached (Fig. S8), which represents the highest reported value for this class of materials under realistic indoor conditions.

This difference in resilience to incident power density can be readily understood by comparing the shunt resistance between both samples (Fig. 4d). Indeed, as the incident power is reduced, the photocurrent diminishes while the shunt current remains roughly constant. Therefore, the detrimental effect of the shunt current becomes increasingly prevalent and significantly reduces performance under low injection conditions. It is therefore essential, when optimising IPV devices, to properly control shunt paths for optimal resilience to variable lighting conditions.

While reporting efficiency is the commonly accepted approach within the PV community, it is in our opinion an incomplete representation of a device performance in the context of indoor PV where the application is to power discrete IoT devices rather than to maximise energy production. Based on a recently published study by our groups, we propose instead, to represent the power generation density of an IPV device ρ_{PGD}^T in mW cm^{-2} as a function of the incident power density at a fixed illumination temperature T, on a similar diagram as the power consumption density of various IoT devices, ρ_{PCD} in mW cm^{-2}, that is, the ratio between the peak

power consumption of an IoT device and its surface area available for IPV. It should be stressed that this approach is incomplete as it assumes a sufficient voltage on the IPV device to be above the threshold of the IoT device. It remains nonetheless a much better representation of the performance of IPV devices under normal operating conditions, where discrete IoT systems should remain powered under variable conditions. More details on the methods can be found in the methodology paper published by our groups.[76] The diagram in Fig. 10 shows the performance of the two previously described devices and compares them with the following IoT devices, using manufacturers data: Philips Hue Motion Sensor, Kona Micro IoT Gateway, and Pressac CO_2 Temperature & Humidity Sensor. The diagram is made using self-developed software, which will be freely shared with the community and is detailed in the aforementioned methodology paper.

Devices differ in their range of applicability, depending on the IoT sensor considered. The Philips Hue Motion sensor, with its low $\rho_{PCD} = 0.01$ mW cm^{-2}, can readily be powered by both IPV devices nearly throughout the entire illumination range, with the exception of very low incident power below ~0.1 mW cm^{-2}. In the case of the Pressac CO_2 sensor ($\rho_{PCD} = 0.12$ mW cm^{-2}), however, the difference in performance between the two

37226 | *J. Mater. Chem. A*, 2025, **13**, 37215–37231

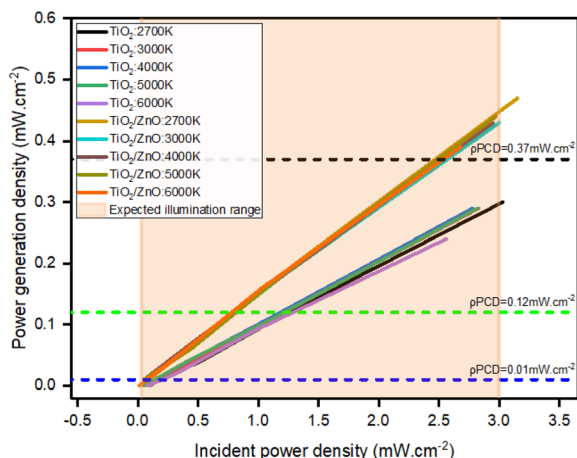This journal is © The Royal Society of Chemistry 2025

Fig. 10 Diagram representing the IPV devices described in this article and three relevant IoT sensors using their power generation density and power consumption density (ρ_{PCD}) respectively as figures of merit; dashed lines coloured in blue, green, and black represent the ρ_{PCD} of the Philips Hue Motion sensor, Pressac CO_2 sensor and Kona Micro IoT Gateway, respectively.

IPV devices leads to a significantly different range of applicability.

Indeed, for the device without ZnO, a light incident power above ~1.25 mW cm^{-2} is required to power the IoT system. When using the IPV device including interfacial ZnO, however, the IoT sensor can be powered with a light incident power as low as ~0.7 mW cm^{-2}. This illustrates how efficiency, while a useful metric in the field of PV, should be repurposed for proper visualisation in the context of IPV and powering IoT devices. Finally, we see that a high light incident power density above 2.5 mW cm^{-2} is necessary to power the Kona Micro IoT Gateway with the IPV device including interfacial ZnO. In contrast the IPV device without ZnO is not capable of powering this IoT system within the expected illumination power range.

In conclusion, the results demonstrate the critical role of interfacial ZnO in enhancing the performance and resilience of IPV under varying lighting conditions. The sample with interfacial ZnO demonstrates superior resilience, maintaining higher efficiency at lower incident power densities compared to the sample without ZnO. This increased stability is essential for powering IoT devices, as demonstrated in the comparison of power generation density with the power consumption of various sensors using a unified diagram focused on power generation density rather than efficiency alone for evaluating IPV devices in real-world applications. These findings demonstrate the importance of reducing shunt paths and shifting the focus of performance evaluation towards a consistent power delivery under diverse indoor conditions.

Experimental section

Materials

FTO substrate (7 Ω sq^{-1}), methanol (99.9 vol%), antimony trichloride (99.99 wt%), thiourea (TU) (99 wt%), chlorobenzene (99.5 vol%), and poly(3-hexylthiophene-2,5-diyl) (P3HT)

(regioregular, >90%) were obtained from Sigma-Aldrich. Titanium(IV) tetraisopropoxide (TTIP) (99 wt%) and acetylacetone – (99 wt%) were purchased from Acros Organics and ethanol (96.6 vol%) was received from Estonian Spirit. Methanol (99.9 vol%, Sigma-Aldrich) and zinc chloride (98 wt%) were used as received.

Fabrication of ZnO-based Sb₂S₃ solar cells

Sb₂S₃ solar cells were assembled with the following structure: FTO/TiO₂/ZnO/Sb₂S₃/P3HT/Au. Initially, pre-cleaned fluorine-doped tin oxide (FTO, ~10 Ω sq^{-1})-covered glass substrates were heated to 340 °C, upon which a thin layer of the TiO₂ ETL was applied by spraying 70 cycles of a 1 : 1 TTIP : acetylacetone molar ratio precursor solution, dissolved in ethanol. The as prepared TiO₂ films were then sintered at 450 °C for 30 min. For the ZnO interface layer, a precursor solution containing a 1 : 2 molar ratio of ZnCl₂ and TU was used, with ZnCl₂ concentration set at (5×10^{-4} M in ethanol). This specific solution concentration was selected based on the research group's previous expertise in fabricating extremely thin NiOₓ layers onto ZnO nanorods by the chemical spray pyrolysis method.[77] We initially intended to deposit ZnS using ZnCl₂ and TU; however, we confirmed the formation of ZnO instead. This unexpected outcome can be attributed to following factors: high catalytic activity of the TiO₂ surface,[78] the open deposition environment, as the deposition process was conducted using USP in air, and the low concentration of TU relative to ZnCl₂, especially considering the relatively high deposition temperature used.[79] The deposition was carried out by using the USP method, typically, 70 cycles of this precursor were sprayed at various surface temperatures (T_s) ranging from 350 to 500 °C. Afterwards, to optimize the thickness of the ZnO layer, we conducted a series of different spraying cycles ranging from 20 to 270 cycles, all deposited at the optimized temperature of 450 °C. Next, Sb₂S₃ absorber layers were ultrasonically sprayed onto both FTO/TiO₂ and FTO/TiO₂/ZnO surfaces. A total of 40 cycles of a 1 : 3 solution of SbCl₃ and TU (60 mM SbCl₃) in methanol were sprayed at a surface temperature of 185 °C. The as obtained amorphous Sb₂S₃ films were rapidly heat annealed at 270 °C under a nitrogen atmosphere for 6 min. For the HTL, 85 μL of 11 mg mL^{-1} P3HT solution was spun coated at 3500 rpm for 20 s and then thermally activated at 150 under nitrogen for 5 min. Finally, superstrate Sb₂S₃ solar cells were coated with an Au contact using the thermal evaporation technique, with a total active device area of 7.063 mm².

Characterization techniques and measurements

Top-view and cross-sectional images of Sb₂S₃ films and solar cells were obtained using a Zeiss EVO-MA15 scanning electron microscope (SEM) equipped with a Zeiss HR FESEM Ultra 55 system. Phase composition of Sb₂S₃ films was characterized by Raman spectroscopy (Horiba Labram HR 800, ~143 μW μm^{-2}, 532 nm YAG:Nd laser). X-ray diffraction (XRD) studies were conducted using a Rigaku Ultima IV system using Cu Kα radiation (λ = 1.54 Å, 40 kV, 40 mA) in the 2θ (Bragg–Brento) configuration, with sample rotation. The measurements were

This journal is © The Royal Society of Chemistry 2025

J. Mater. Chem. A, 2025, **13**, 37215–37231 | **37227**

performed with a 2θ step of 0.02° and a counting time 2–10 s per step. Then the obtained diffraction patterns were compared with JCPDS 01-075-4012. The surface composition of the ZnO interlayer and Sb_2S_3 absorber layer was investigated by X-ray photoelectron spectroscopy (XPS) using a Thermo Fisher ESCALAB Xi XPS/UPS system equipped with Al Kα radiation ($h\nu$ = 1486.6 eV).

Solar cell performance was evaluated by measuring J–V curves in forward bias using an AUTOLAB PGSTAT 30. The measurement was conducted under 100 mW cm^{-2} illumination, provided by a calibrated solar simulator (Wavelabs LS2, LED light source). EBSD maps were acquired using a Zeiss UltraPlus scanning electron microscope equipped with an Oxford Instruments Symmetry EBSD detector at 15 keV and about 6 nA. The maps were recorded and analyzed using the AZtec software suite. Modulated SPV spectra were measured in fixed capacitor mode. Samples were illuminated from the top surface using a double prism monochromator (DPM100) coupled with a laser driven light source (EQ-99X) in the photon energy range 0.6–4 eV. The illumination was modulated by a chopper at a frequency of 8 Hz. EQE spectra were detected by using a monochromatic light source (Newport 300 W xenon lamp, 69911 with a Cornerstone 260 monochromator), equipped with a digital lock-in detector (Merlin), and a calibrated Si reference detector.

For band alignment diagram construction, X-ray photoelectron spectroscopy was conducted in an ultra-high vacuum (UHV) chamber operating at a base pressure of 1×10^{-9} mbar. Core-levels and the valence band were probed using a SPECS monochromatic Al Kα X-ray source ($h\nu$ = 1486.6 eV). The experiments were performed at a power of 180 W, using a PSP Vacuum Technology electron-energy analyser operating at a pass energy of 10 eV. The secondary electron cutoff (SEC) measurements were carried out at a lower operating power of 15 W and a pass energy of 2 eV. A -10 V bias was applied to the sample to separate the spectrometer response. The core levels were fitted using Casa XPS software, and the spectrum was calibrated to a C 1s value of 285 eV. Analysis of the SEC and VBM for TiO_2 and $TiO_2/ZnO/Sb_2S_3$ surfaces is provided in SI Fig. S7, with a linear fit applied to the background and the cut-offs to calculate the work function and ionization potential. With the bandgap known, the conduction band minimum was then derived. Bandgap values were extracted from squared SPV amplitude spectra for both TiO_2 and TiO_2/ZnO and from Tauc plots for Sb_2S_3.

Absolute PL measurements were conducted using a home-built absolute PL set-up equipped with a 405 nm laser excitation source at room temperature, and a CCD Si detector.[80] The experimental setup was first calibrated, and the resulting spectra were corrected both spectrally and in intensity, as described in ref. 81 The incident photon flux was initially set to correspond to the 1 sun photon flux received by an absorber with a bandgap of 1.7 eV under AM 1.5 illumination. However, no signal was detected under 1 sun conditions; therefore, the excitation power was increased to the maximum output of the laser diode and focussed through a lens, resulting in an incident power of approximately 160 suns on the sample. The Y_{PL}

was calculated using the relation, $Y_{PL} = \Phi_{PL}/\Phi_{laser}$, where Φ_{PL} represents the integrated PL flux of the near-band edge (NBE) emission peak between 1.56 eV and 1.65 eV, and Φ_{laser} represents the incident photon flux. To prevent any reflection, the semi-transparent Sb_3S_3 sample was secured to the sample holder using carbon tape, which exhibits negligible reflection when exposed to the laser source. Since the expected emission peak at 1.7 eV overlaps with the spectral region of the glass substrate, reference measurements were performed (i.e. on quartz/TiO_2 and quartz/TiO_2/ZnO coated substrates) to isolate the emission contribution from the Sb_2S_3 thin film. Additionally, high reflection from the second-order laser signal near the NBE emission peak rendered the NBE peak less distinguishable.

Deep level transient spectroscopy (DLTS) analysis was conducted using a Phystech FT1230 HERA DLTS system connected to a Linkam HFSX350 liquid nitrogen fed cryostat in a temperature range of 80–300 K. Capacitance transients were generated using reverse and pulse biases of 6 V and 0.5 V respectively with a pulse duration of 1 ms. The resultant transients were compared over three period widths of 19.2, 192 and 480 ms with values for the trap energies and capture cross section extracted from an Arrhenius assessment using the three period widths and by fitting a multi-exponential function to the capacitance transients.

Indoor characterisation was performed using a Keithley 6430 sourcemeter and a G2V Pico solar simulator controlled with a self-developed script (Z. Jehl Li-Kao, UPC) allowing to adjust the spectrum to match that of LED light sources of various temperatures. The real incident power in each condition was measured using a Thorlabs PM100D power meter and a S120VC Standard Photodiode Power Sensor, and the relative accuracy of the measurement was estimated to be ±4%. We deliberately chose to report the conditions in units of power density rather than in Lux, as the latter is based on human vision and has little scientific value beyond its marketing use by bulb manufacturers. Moreover, we observed that most commercial Lux meters are highly inaccurate and using such units in the context of a scientific publication may encourage other groups to use inaccurate calibration devices. We provide nonetheless a simple self-developed script[82] to calculate the Lux value of any spectrum, for readers interested in doing so. The diagram comparing the power generation density of IPV and the power consumption density of IoT devices was made with a self-developed script (Z. Jehl Li-Kao, UPC). The executable version of the script, discussed in more detail in the aforementioned methodology paper published by the groups involved in the present manuscript, can be found here: **https://doi.org/10.5281/zenodo.14226891**. The surface plots of IPV performance are realized with the condition mesh shown in Tables S5a and b.

Conclusion

In conclusion, this study investigated the effect of ZnO as an interfacial layer on the performance of in-air ultrasonic sprayed Sb_2S_3 solar cells. We conducted a series of optimization processes for the ZnO layer by varying both the deposition temperature and the number of spraying cycles. Our findings

37228 | J. Mater. Chem. A, 2025, 13, 37215–37231

This journal is © The Royal Society of Chemistry 2025

reveal the vital role of ZnO for improving the quality of the TiO_2/Sb_2S_3 interface and controlling the growth of the Sb_2S_3 absorber. Increasing the spraying cycles to 150 cycles at a fixed deposition temperature of 450 °C yielded a thicker absorber layer compared to deposition directly on top of TiO_2, as observed in cross-sectional SEM images, indicating that the presence of ZnO leads to higher growth rates of Sb_2S_3 films. Additionally, EBSD, SPV and PL measurements proved the effectiveness of ZnO in reducing grain boundary density, passivating TiO_2 and reducing non-radiative recombination at the interface between TiO_2 and ZnO, which are key factors for V_{OC} enhancement. In agreement with these findings, the XPS based band alignment suggests that ZnO have an impact on interface recombination suppression. DLTS analysis revealed that, regardless of the nature of the observed defects and the performance benefits provided by the additional interface layer, their role as recombination centres suggests that improved material quality for Sb_2S_3 is achievable. These cumulative improvements led to the highest device performance of 7.5%, recorded for TiO_2 based Sb_2S_3 solar cells, featuring a 150 nm absorber—the thinnest Sb_2S_3 absorber delivering such performance to date. Furthermore, the optimized ZnO based Sb_2S_3 solar cell achieved an IPV efficiency of 18% under 6200 mW cm^{-2} WLED illumination power density. This device demonstrated notable resilience and stability under low-light illumination, retaining an efficiency of 12.3% even at an incident power as low as 50 mW cm^{-2}, which is essential for powering IoT devices. The proposed refinements to indoor measurement protocols, which account for a wide array of lighting conditions, including variations in source temperature and incident power, pave the way for more reliable indoor PV performance evaluation, enabling consistent power delivery under diverse indoor conditions.

Author contributions

H. Hussien: writing – original draft preparation, investigation, conceptualization, validation, visualization, methodology, formal analysis. M. Krunks: investigation, conceptualization, writing – review & editing, visualization, validation, project administration, formal analysis. N. Spalatu: writing – review & editing, visualization, investigation, funding acquisition. A. Katerski: visualization, validation, methodology, investigation, formal analysis. Z. Jehl Li-Kao: writing – review & editing, visualization, investigation, methodology, formal analysis. S. Giraldo: writing – review & editing, visualization, investigation, methodology, formal analysis. D. Abou-Ras: writing – review & editing, visualization, investigation, methodology, formal analysis. A. Valluvar Oli: writing – review & editing, visualization, investigation, methodology, formal analysis. S. Siebentritt: writing – review & editing, visualization, investigation, methodology, formal analysis. J. D. Major: writing – review & editing, visualization, investigation, methodology, formal analysis. A. A. Almushawwah: visualization, validation, methodology, formal analysis. T. P. Shalvey: visualization, validation, methodology, formal analysis. R. Grzibovskis: visualization, validation, methodology, formal analysis. A. Vembris: visualization, validation, methodology, formal analysis. I. Oja Acik: investigation, conceptualization, writing – review & editing, validation, supervision, project administration, funding acquisition, formal analysis.

Conflicts of interest

The authors declare no conflict of interest.

Data availability

The data supporting this article have been included as part of the supplementary information (SI). Supplementary information is available. See DOI: https://doi.org/10.1039/d5ta05790f.

Acknowledgements

References

1 A. Chakraborty, G. Lucarelli, J. Xu, Z. Skafi, S. Castro-Hermosa, A. B. Kaveramma, R. G. Balakrishna and T. M. Brown, *Nano Energy*, 2024, **128**, 109932.

2 Q. Ma, Y. Wang, L. Liu, P. Yang, W. He, X. Zhang, J. Zheng, M. Ma, M. Wan, Y. Yang, C. Zhang, T. Mahmoudi, S. Wu, C. Liu, Y. B. Hahn and Y. Mai, *Energy Environ. Sci.*, 2024, **17**, 1637–1644.

This journal is © The Royal Society of Chemistry 2025

J. Mater. Chem. A, 2025, **13**, 37215–37231 | **37229**

3 C. H. Chen, S. N. Cheng, L. Cheng, Z. K. Wang and L. S. Liao, *Adv. Energy Mater.*, 2023, **13**, 2204144.

4 J. Chen, G. Li, Z. Xu, C. Xu, F. Naveed, B. Liu, Y. Zhang, R. Zhou, C. Chen, M. Wang, J. Xu and L. Li, *Adv. Funct. Mater.*, 2024, **34**, 2313676.

5 U. A. Shah, S. Chen, G. M. G. Khalaf, Z. Jin and H. Song, *Adv. Funct. Mater.*, 2021, **31**, 2100265.

6 S. Wang, Y. Zhao, B. Che, C. Li, X. Chen, R. Tang, J. Gong, X. Wang, G. Chen, T. Chen, J. Li and X. Xiao, *Adv. Mater.*, 2022, **34**, 2206242.

7 X. Chen, Y. Zhao, C. Li, X. Wang, P. Xiao, J. Gong, T. Chen, X. Xiao and J. Li, *Adv. Energy Mater.*, 2024, **14**, 2400441.

8 J. Zheng, C. Liu, L. Zhang, Y. Chen, F. Bao, J. Liu, H. Zhu, K. Shen and Y. Mai, *Chem. Eng. J.*, 2022, **446**, 2206242.

9 R. Cao, K. Lv, C. Shi, Y. Wang, C. Ye, F. Guo, G. Hu and W. Chen, *ACS Appl. Mater. Interfaces*, 2024, **16**, 42513–42521.

10 G. Hu, C. Shi, B. Yang, Z. Wang, K. Lv, Y. Wang, F. Guo and W. Chen, *Mater. Today Energy*, 2024, **45**, 101670.

11 H. Gao, J. Li, X. Peng, Y. Huang, Q. Zhao, H. Wang, T. Wu, S. Sheng, R. Tang and T. Chen, *Sol. RRL*, 2024, **8**, 2400389.

12 X. Chen, X. Shu, J. Zhou, L. Wan, P. Xiao, Y. Fu, J. Ye, Y.-T. Huang, B. Yan, D. Xue, T. Chen, J. Chen, R. L. Z. Hoye and R. Zhou, *Light: Sci. Appl.*, 2024, **13**, 281.

13 X. Li, A. A. Shah, M. Abbas, J. Hu, Z. Zheng, S. Chen, Z. Su, J. Zhao, M. Ishaq and G. Liang, *ACS Appl. Energy Mater.*, 2024, **7**, 5848–5856.

14 R. Zhou, B. Tang, Q. Xie, W. Wu, L. Wan, S. J. Zelewski and J. Zhu, *Appl. Phys. Lett.*, 2024, **124**, 233903.

15 R. Zhou, B. Guo, W. Wu, H. Wang, H. Niu and L. Wan, *IEEE Trans. Electron Devices*, 2024, **71**, 7609.

16 J. Han, X. Pu, H. Zhou, Q. Cao, S. Wang, Z. He, B. Gao, T. Li, J. Zhao and X. Li, *ACS Appl. Mater. Interfaces*, 2020, **12**, 44297–44306.

17 C. Wu, L. Zhang, B. Che, P. Xiao, J. Yang, H. Wang, L. Chu, W. Yan and T. Chen, *J. Mater. Chem. A*, 2023, **11**, 8184–8191.

18 K. Li, R. Tang, C. Zhu and T. Chen, *Adv. Sci.*, 2024, **11**, 2304963.

19 Z. Peng, Q. Zheng, R. Wang, L. Sun, H. Wang, Y. Yuan, Y. Xing, L. Yao, J. Bi and W. Li, *Sol. Energy Mater. Sol. Cells*, 202, **253**, 112208.

20 X. Liu, Z. Cai, L. Wan, P. Xiao, B. Che, J. Yang, H. Niu, H. Wang, J. Zhu, Y. T. Huang, H. Zhu, S. J. Zelewski, T. Chen, R. L. Z. Hoye and R. Zhou, *Adv. Mater.*, 2024, **36**, 2305841.

21 M. A. Farhana, A. Manjceevan, H.-Y. Tan, C.-F. Yan and J. Bandara, *Opt. Quantum Electron.*, 2023, **55**, 678.

22 R. Kondrotas, C. Chen and J. Tang, 2018, **2**, pp. 857–878.

23 S. Rühle, *Sol. Energy*, 2016, **130**, 139–147.

24 M. F. Müller, M. Freunek and L. M. Reindl, *IEEE J. Photovolt.*, 2013, **3**, 59–64.

25 J. K. W. Ho, H. Yin and S. K. So, *J. Mater. Chem. A*, 2020, **8**, 1717–1723.

26 A. Mavlonov, T. Razykov, F. Raziq, J. Gan, J. Chantana, Y. Kawano, T. Nishimura, H. Wei, A. Zakutayev, T. Minemoto, X. Zu, S. Li and L. Qiao, *Sol. Energy*, 2020, **201**, 227–246.

27 C. Li, H. Sun, D. Dou, S. Gan and L. Li, *Adv. Energy Mater.*, 2024, **14**, 2401883.

28 X. Zhang, J. Pascual, Z. Li, X. Zhang, Z. Su, J. Zhang, X. Gao, B. Hou, G. Li, A. Abate and M. Li, *Sci. Bull.*, 2025, **70**, 556–562.

29 P. Büttner, F. Scheler, C. Pointer, D. Döhler, T. Yokosawa, E. Spiecker, P. P. Boix, E. R. Young, I. Mínguez-Bacho and J. Bachmann, *ACS Appl. Mater. Interfaces*, 2021, **13**, 11861–11868.

30 O. A. Jaramillo-Quintero, A. Baron-Jaimes, R. A. Miranda-Gamboa and M. E. Rincon, *Sol. Energy*, 2021, **224**, 697–702.

31 W. Lin, W. T. Guo, L. Yao, J. Li, L. Lin, J. M. Zhang, S. Chen and G. Chen, *ACS Appl. Mater. Interfaces*, 2021, **13**, 45726–45735.

32 O. A. Jaramillo-Quintero, Y. A. Alarcón-Altamirano, R. A. Miranda-Gamboa and M. E. Rincón, *Appl. Surf. Sci.*, 2020, **526**, 146705.

33 J. S. Eensalu, S. Mandati, C. H. Don, H. Finch, V. R. Dhanak, J. D. Major, R. Grzibovskis, A. Tamm, P. Ritslaid, R. Josepson, T. Käämbre, A. Vembris, N. Spalatu, M. Krunks and I. Oja Acik, *ACS Appl. Mater. Interfaces*, 2023, **15**, 42622–42636.

34 J. S. Eensalu, A. Katerski, E. Kärber, L. Weinhardt, M. Blum, C. Heske, W. Yang, I. O. Acik and M. Krunks, *Beilstein J. Nanotechnol.*, 2019, **10**, 2396–2409.

35 Z. Feng, S. Sun, Y. Sun, X. Liu, H. Liu and H. Liu, *Appl. Phys. A: Mater. Sci. Process.*, 2022, **128**, 479.

36 P. S. Pawar, R. Nandi, K. Rao Eswar Neerugatti, I. Sharma, R. Kumar Yadav, Y. Tae Kim, J. Yu Cho and J. Heo, *Sol. Energy*, 2022, **246**, 141–151.

37 C. Liu, Z. Cao, W. Cheng, Y. Liu, Y. Liu, Y. Dai, J. Dong, J. Li, X. Xu and Y. Zhang, *J. Chem. Phys.*, 2025, **162**, 204704.

38 P. Kaienburg, P. Hartnagel, B. E. Pieters, J. Yu, D. Grabowski, Z. Liu, J. Haddad, U. Rau and T. Kirchartz, *J. Phys. Chem. C*, 2018, **122**, 27263–27272.

39 T. P. Shalvey, C. H. Don, L. Bowen, T. D. Veal and J. D. Major, *Adv. Mater. Interfaces*, 2024, **11**, 2400394.

40 P. Büttner, F. Scheler, D. Döhler, M. K. S. Barr, M. Bosch, M. Rey, T. Yokosawa, S. Hinz, J. Maultzsch, E. Spiecker, N. Vogel, I. Mínguez-Bacho and J. Bachmann, *Nano Energy*, 2022, **103**, 107820.

41 G. B. Harris, *The London, Edinburgh, and Dublin Philosophical Magazine and Journal of Science*, 1952, vol. 43, pp. 113–123.

42 A. L. Patterson, *The Scherrer Formula for I-Ray Particle Size Determination*, 1939, vol. 56.

43 D. A. H. Hanaor and C. C. Sorrell, *J. Mater. Sci.*, 2011, **46**, 855–874.

44 H. Zhang and J. F. Banfield, *Materials Thermodynamic Analysis of Phase Stability of Nanocrystalline Titania*, 1998, vol. 8.

45 F. Zahedi, R. S. Dariani and S. M. Rozati, *Mater. Sci. Semicond. Process.*, 2013, **16**, 245–249.

46 T. Dedova, M. Krunks, I. Gromyko, V. Mikli, I. Sildos, K. Utt and T. Unt, *Phys. Status Solidi A*, 2014, **211**, 514–521.

47 V. Raj, T. Haggren, Y. O. Mayon, C. Jagadish and H. H. Tan, *Sol. RRL*, 2024, **8**, 2300889.

37230 | *J. Mater. Chem. A*, 2025, **13**, 37215–37231

This journal is © The Royal Society of Chemistry 2025

48 M. Ishaq, S. Chen, U. Farooq, M. Azam, H. Deng, Z. H. Su, Z. H. Zheng, P. Fan, H. S. Song and G. X. Liang, *Sol. RRL*, 2020, **4**, 2000551.

49 L. Jiang, J. Li, K. Huang, S. Li, Q. Wang, Z. Sun, T. Mei, J. Wang, L. Zhang, N. Wang and X. Wang, *ACS Omega*, 2017, **2**, 8990–8996.

50 A. Ghobadi, T. G. U. Ghobadi, F. Karadas and E. Ozbay, *Sci. Rep.*, 2018, **8**, 16322.

51 H. Ma, B. Hao, W. Song, J. Guo, M. Li and L. Zhang, *Materials*, 2021, **14**, 3299.

52 K. Shen, K. Wu and D. Wang, *Mater. Res. Bull.*, 2014, **51**, 141–144.

53 K. C. Gödel, Y. C. Choi, B. Roose, A. Sadhanala, H. J. Snaith, S. Il Seok, U. Steiner and S. K. Pathak, *Chem. Commun.*, 2015, **51**, 8640–8643.

54 C. Jiang, R. Tang, X. Wang, H. Ju, G. Chen and T. Chen, *Sol. RRL*, 2019, **3**, 1800272.

55 U. Chime, L. Wolf, V. Buga, D. Weigand, A. Gad, J. Köhler, A. Lambertz, W. Duan, K. Ding, T. Merdzhanova, U. Rau and O. Astakhov, *Sol. RRL*, 2022, **6**, 2100594.

56 M. Mohan, V. Nandal, S. Paramadam, K. P. Reddy, S. Ramkumar, S. Agarwal, C. S. Gopinath, P. R. Nair and M. A. G. Namboothiry, *J. Phys. Chem. C*, 2017, **121**, 5523–5530.

57 S. Lee, S. Kim, S. Shin, Z. Jin and Y.-S. Min, *J. Ind. Eng. Chem.*, 2018, **58**, 328–333.

58 S. S. Wilson, J. P. Bosco, Y. Tolstova, D. O. Scanlon, G. W. Watson and H. A. Atwater, *Energy Environ. Sci.*, 2014, **7**, 3606–3610.

59 J. S. Eensalu, A. Katerski, E. Kärber, L. Weinhardt, M. Blum, C. Heske, W. Yang, I. O. Acik and M. Krunks, *Beilstein J. Nanotechnol.*, 2019, **10**, 2396–2409.

60 J. S. Eensalu, A. Katerski, E. Kärber, I. O. Acik, A. Mere and M. Krunks, *Beilstein J. Nanotechnol.*, 2019, **10**, 198–210.

61 Y. Diao, A. S. Myerson, T. A. Hatton and B. L. Trout, *Langmuir*, 2011, **27**, 5324–5334.

62 J. Li, L. Xiong, X. Hu, J. Liang, C. Chen, F. Ye, J. Li, Y. Liu, W. Shao, T. Wang, C. Tao and G. Fang, *J. Energy Chem.*, 2022, **66**, 374–381.

63 X. Li, J. Wang, T. Wang, N. Wang, S. Zong, X. Huang and H. Hao, *Sci. China: Chem.*, 2021, **64**, 1460–1481.

64 G. S. Rohrer, *Introduction to grains, phases, and interfaces - An interpretation of microstructure*, 2010, DOI: **10.1007/s11663-010-9364-6**.

65 K. Ellmer and A. Bikowski, *J. Phys. D: Appl. Phys.*, 2016, **49**, 413002.

66 V. C. Anitha, A. N. Banerjee and S. W. Joo, *J. Mater. Sci.*, 2015, **50**, 7495–7536.

67 J. Mattheis, U. Rau and J. H. Werner, *J. Appl. Phys.*, 2007, **101**, 113519.

68 S. Siebentritt, U. Rau, S. Gharabeiki, T. P. Weiss, A. Prot, T. Wang, D. Adeleye, M. Drahem and A. Singh, *Faraday Discuss.*, 2022, **239**, 112–129.

69 U. Rau, *Phys. Rev. B: Condens. Matter Mater. Phys.*, 2007, **76**, 085303.

70 U. Rau, B. Blank, T. C. M. Müller and T. Kirchartz, *Phys. Rev. Appl.*, 2017, **7**, 044016.

71 A. R. Peaker, V. P. Markevich and J. Coutinho, *J. Appl. Phys.*, 2018, **123**, 161559.

72 L. Dobaczewski, A. R. Peaker and K. Bonde Nielsen, *J. Appl. Phys.*, 2004, **96**, 4689–4728.

73 S. W. Provencher, *Comput. Phys. Commun.*, 1982, **27**, 229–242.

74 J. Lauwaert, S. Khelifi, K. Decock, M. Burgelman and H. Vrielinck, *J. Appl. Phys.*, 2011, **109**, 063721.

75 X. Wang, Z. Li, S. R. Kavanagh, A. M. Ganose and A. Walsh, *Phys. Chem. Chem. Phys.*, 2022, **24**, 7195–7202.

76 M. Placidi, A. Torrens, Z. Jehl Li-Kao, A. Lopez-Garcia, O. Segura, Y. Gong, A. Jimenez-Arguijo, I. Caño, S. Giraldo, E. Saucedo, G. Alvarez, Y. Sanchez, N. Spalatu, I. Oja, E. Artegiani, A. Romeo, R. Scaffidi and A. Perez-Rodriguez, *Sol. RRL*, 2025, **9**, 202500030.

77 Z. Chen, T. Dedova, N. Spalatu, N. Maticiuc, M. Rusu, A. Katerski, I. O. Acik, T. Unold and M. Krunks, *Colloids Surf., A*, 2022, **648**, 129366.

78 J. Spiridonova, A. Katerski, M. Danilson, M. Krichevskaya, M. Krunks and I. O. Acik, *Molecules*, 2019, **24**, 4326.

79 B. Su and K. L. Choy, *J. Mater. Chem.*, 2000, **10**, 949–952.

80 S. Siebentritt, T. P. Weiss, M. Sood, M. H. Wolter, A. Lomuscio and O. Ramirez, *J. Phys.: Mater.*, 2021, **4**, 042010.

81 A. J. M. Prot, M. Melchiorre, F. Dingwell, A. Zelenina, H. Elanzeery, A. Lomuscio, T. Dalibor, M. Guc, R. Fonoll-Rubio, V. Izquierdo-Roca, G. Kusch, R. A. Oliver and S. Siebentritt, *APL Mater.*, 2023, **11**, 101120.

82 Z. Jehl Li-Kao and K. Tiwari, *Light Spectrum Converter (6.5)*, Zenodo, 2025, DOI: **10.5281/zenodo.14795263**.

This journal is © The Royal Society of Chemistry 2025

J. Mater. Chem. A, 2025, **13**, 37215–37231 | **37231**